

Polyethylene Glycol–Na⁺ Interface of Vanadium Hexacyanoferrate Cathode for Highly Stable Rechargeable Aqueous Sodium-Ion Battery

Ping Jiang,^{†,‡,⊥,♯} Zhenyu Lei,^{†,♯} Liang Chen,[‡] Xuecheng Shao,^{||} Xinmiao Liang,[†] Jun Zhang,[‡] Yanchao Wang,^{||} Jiujun Zhang,^{*,§,⊥} Zhaoping Liu,^{*,‡,⊥} and Jiwen Feng^{*,†,⊥}

[†]Wuhan Institute of Physics and Mathematics, Chinese Academy of Sciences, Wuhan 430071, P.R. China

[‡]Ningbo Institute of Materials Technology and Engineering, Chinese Academy of Sciences, Ningbo 315201, P.R. China

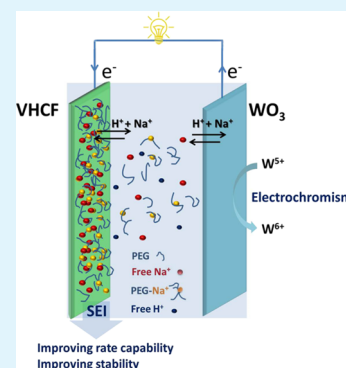
[§]Institute for Sustainable Energy/College of Sciences, Shanghai University, Shanghai 200444, P.R. China

^{||}State Key Laboratory of Superhard Materials, College of Physics, Jilin University, Changchun 130012, P.R. China

[⊥]University of Chinese Academy of Sciences, Beijing 100000, P.R. China

Supporting Information

ABSTRACT: Vanadium hexacyanoferrate (VHCF) with an open-framework crystal structure is a promising cathode material for rechargeable aqueous metal-ion batteries owing to its high electrochemical performance and easy synthesis. In this paper, vanadium hexacyanoferrate cathodes were first used for constructing rechargeable aqueous sodium-ion batteries (VHCF/WO₃) and tested in the new-type electrolyte (NaP-4.6) consisting of a polyethylene glycol (PEG)/H₂O/NaClO₄ electrolyte with a low H⁺ concentration (molar ratio of [H₂O]/[Na⁺] is 4.6), which has high stability at a high current density as high as 1000 mA g⁻¹ with a capacity retention of 90.3% after 2000 cycles at high coulombic efficiency (above 97.8%). To understand their outstanding performance, the proton-assisted sodium-ion storage mechanism and interphase chemistry of VHCF are investigated by solid-state NMR (ssNMR) technology. It is suggested that the H⁺ storage reaction is accompanied by the redox of vanadium atoms and Na⁺ intercalation is accompanied by the redox of iron atoms. It is also observed that the complex of polyethylene glycol (PEG) with Na⁺ (PEG–Na⁺) exists on the VHCF surface, which facilitates the stability of VHCF and promotes the alkali-ion transfer at a high current density. The results of the ssNMR study offer new insights into the intercalation chemistry of Prussian blue analogues with open-framework-structured compounds, which can greatly broaden our horizons for battery research.



KEYWORDS: Vanadium hexacyanoferrate, Solid electrolyte interphase, Solid-state NMR, Aqueous rechargeable sodium-ion battery

1. INTRODUCTION

Rechargeable batteries have been recognized to be the most reliable, highly efficient, and practical device for storage of renewable electrical energy generated from sustainable sources such as solar, wind, sea wave/tide, and water reserves.^{1–4} Current nonaqueous lithium-based batteries have been widely employed in portable electronics, electric vehicles, and electrical grids but suffer from flammable, volatile, and toxic electrolytes.¹ Thus, high-performance rechargeable aqueous ion batteries (RAIB), which can substitute the commercial lead-acid, Ni-MH, or Ni-Cd aqueous battery, are considered to be a type of optimal energy storage device because of their expected better safety, lower cost, and being more environmentally friendly.⁴ To date, RAIBs with Li⁺ shuttles have been extensively explored,⁵ but Na⁺ ions as shuttle ions are of greater interest due to the higher abundance and lower cost of the sodium resource.⁶ However, only a few types of RAIBs based on sodium ions have been reported due to the fact that cathode and anode materials allowing the reversible reaction of

Na⁺ in aqueous electrolytes are very limited. Recently, Prussian blue analogues (PBAs) with the general formula of A_xM_k[M'(CN)₆]_n·mH₂O (A = alkali cation ion, M and M' = transition-metal ions) have been explored as promising intercalation compounds for cathode materials in rechargeable batteries,^{7–18} and their large open frameworks are readily accessible for unitary electroactive ions (e.g., H⁺ (or H₃O⁺), Li⁺, Na⁺, K⁺, or Zn²⁺, and dual cations). For example, RAIBs of M[Fe(CN)₆]/NaTi₂(PO₄)₃ (M = Cu, Ni, Co, In, Zn) systems based on Na⁺ or K⁺ shuttles^{7,10,15,17,18} have been reported for their high operation voltage (>1.2 V), but the low specific capacity (less than 60 mA h g⁻¹) and poor cyclic performance, which is due to the defects in the PBA crystal structure, have limited their application in aqueous energy storage devices. Thus, high-performance electrode materials that are compat-

Received: March 18, 2019

Accepted: July 18, 2019

Published: July 18, 2019

ible with aqueous systems are required for potential application.

Considering that the electrochemical process of PBA highly depends on the redox process of the metal ions upon insertion/extraction of ions, it is crucial to improve the solid/electrolyte interface of the electrode^{19–21} or optimize the combination of transition-metal ions for enhancing the electrochemical performance. Vanadium hexacyanoferrate (VHCF)-based PBA materials have been reported to be used for Na⁺ battery electrodes,^{22,23} but their structural defects and abnormal arrangement of cations in the VHCF lattice could result in a rapid capacity attenuation during the three-electrode cycling test.

In this work, vanadium hexacyanoferrate (VHCF) is prepared with a perfect cubic structure by a simple coprecipitation method and first used as the cathode electrodes for a rechargeable sodium-ion battery (VHFC/NaP-4.6/WO₃). A new-type electrolyte containing HClO₄, NaClO₄, and an appropriate amount of polyethylene glycol (PEG) is used for the battery. The molar ratio of [Na⁺]/[H₂O] in the electrolyte is maintained at 1:4.6.⁷ The added PEG can assist the formation of the solid electrolyte interphase (SEI) on the VHCF electrode, improving its rate capability and cycle life. The proton-assisted Na⁺-intercalation mechanism involving the open framework of the VHCF electrode is directly unveiled by the solid-state MAS NMR spectra.

2. EXPERIMENTAL SECTION

2.1. Vanadium Hexacyanoferrate (VHCF) Synthesis. VHCF was synthesized by the coprecipitation method. Typically, 100 mL of 0.05 M K₃Fe(CN)₆ (Aladdin) and 100 mL of 0.1 M VOSO₄ (Sigma) were simultaneously added into 100 mL of water solution under stirring. The dropping rates of VOSO₄ and K₃Fe(CN)₆ solutions were precisely controlled by a peristaltic pump (0.3 mL min⁻¹). After the reaction was completed, the light green VHCF slurry was obtained. Finally, the precipitate was washed with deionized water several times and then dried at 80 °C overnight; thus, 1.41 g of VHCF was obtained. The prepared VHCF electrodes at different cutoff voltages (States a to g) during charging/discharging processes were obtained for solid-state NMR measurements. The test samples were addressed as follows: (i) for the electrode samples without washing, the samples were just cleaned with mirror paper and vacuum-oven-dried at 100 °C; (ii) for the electrode samples with washing, the samples were washed with ethanol many times and vacuum-oven-dried 100 °C for 10 h.

2.2. Tungsten Trioxide (WO₃) Synthesis. WO₃ was synthesized by the electrodeposition method. Typically, 1.03 g of Na₂WO₄·2H₂O was dissolved in 250 mL of deionized water, and 2 mL of perchloric acid and 0.65 mL of H₂O₂ were added to the solution under stirring. The WO₃ film was prepared by continuous electrodeposition for 10 min on an indium tin oxide (ITO)-coated glass substrate, which was performed with a Solartron 1470E electrochemical workstation (Farnborough, U.K.) at room temperature using a conventional three-electrode system, and ITO-glass, a 2 × 2 cm² platinum foil, and an Ag/AgCl electrode were used as the working electrode, the counter electrode, and the reference electrode, respectively. After deposition, the film was thoroughly washed with ethanol and water and dried in air. Then 0.25% Nafion solution dissolved in ethanol was dipped evenly over the surface of the WO₃ film and dried in air.

2.3. Electrolyte Preparation. NaClO₄ electrolytes were prepared by dissolving 6.84 g of NaClO₄·H₂O (Aladdin) in 7 g of polyethylene glycol (PEG, Aladdin, M_w = 400) and 2.86, 4.91, and 7.58 g H₂O; then 1 g of HClO₄ (Sinopharm Chemical Reagent, 70 wt %) was added to the above three solutions to obtain solutions with three different molar ratios of [H₂O]/[Na⁺] (4.6, 7, and 9, respectively), which are abbreviated as NaP-4.6, NaP-7, and NaP-9. The acid concentrations of such solutions are all about 0.5 M. For comparison,

0.5 M HClO₄ in the saturated NaClO₄ electrolyte without adding PEG was also prepared, named Sat-Na, with a [H₂O]/[Na⁺] molar ratio of about 7.

2.4. Characterization. Powder X-ray diffraction patterns were collected using an AXS D8 Advance diffractometer (Cu K α radiation; receiving slit, 0.2 mm; scintillation counter, 40 mA; 40 kV) from Bruker Inc. The morphology and structure of samples were analyzed by a Hitachi S-4800 field emission scanning electron microscope at an accelerating voltage of 200 kV. The contents of V, Fe, and K atoms in VHCF were detected by inductively coupled plasma emission spectrometry (ICP-OES) using a PE Optima 2100DV. Raman spectra were collected with a Renishaw in Via Reflex confocal microscopy Raman spectrometer using 532 nm at laser wavenumbers from 4000 to 500 cm⁻¹ for all the samples. The chemical bonding of VHCF was obtained by using infrared spectra FT-IR (Nicolet 6700) with KBr powder-pressed pellets. Ex situ multinuclear ssNMR spectra were obtained on 9.4 T Bruker Avance 500 MHz spectrometers. Magic-angle spinning (MAS) frequencies ranged from 10 to 60 kHz, spinning under N₂. Several electrode samples (of 65 to 90 mg) were filled to the 4 mm rotors and enhanced the signal in the experiments. ¹H chemical shifts were externally referenced to adamantane (¹H 1.9 ppm) and ²³Na to 1 M NaCl (0 ppm). ¹H and ²³Na solid-state nuclear magnetic resonance (NMR) spectra were acquired. All NMR measurements were conducted at room temperature.

2.5. Electrochemical Measurements. Electrochemical measurements were carried out on Solartron 1470E multichannel potentiostats using a three-electrode cell setup. A VHCF-material-coated Ti grid substrate, a Ag/AgCl electrode (0.2 V vs SHE), and a Pt gauze were employed as the working electrode, reference electrode, and counter electrodes, respectively. The working electrodes were prepared by mixing the corresponding VHCF slurries (75 wt %), Super P (15 wt %), and polyvinylidene fluoride (10 wt %) in *n*-methyl-2-pyrrolidinone on the Ti grid disc with a diameter of 13 mm and air-dried at 80 °C. The VHCF mass loadings on the electrodes were about 6 mg. To validate the VHFC cathodes and the aqueous electrolyte, a battery consisting of the VHFC cathode, NaP-4.6 electrolyte, and WO₃ anode was constructed for the battery performance tests. The mass ratio of VHFC/WO₃ was about 1:1.

3. RESULTS AND DISCUSSION

3.1. Structure and Chemical Properties of Vanadium Hexacyanoferrate. Vanadium hexacyanoferrate (VHCF) was synthesized by a coprecipitation method through controlling the molar ratio of the precursor solution. VHCF showed better crystallinity when the molar ratio of V/Fe = 2:1 (see Figure S1). The powder X-ray diffraction patterns (XRD) of the obtained VHCF in Figure 1a and Figure S1 show that VHCF exhibits a similar cubic structure analogous to that of Prussian blue.^{10,12,15,17,18,24,25} The ab initio structure predictions in Figure 1 and Figure S2 for VHCF were calculated using the particle swarm optimization technique, which is implemented in the CALYPSO code.^{26–29} Figure 1b shows the octahedral structure model of VO(NC)₅ and Fe(CN)₆, which are linked by sharing CN ligands in the VHCF crystallographic structure, about 33% sites of the Fe(CN)₆ complex are vacant, and the vanadium ions are coordinated by five bridging C=N groups and one oxygen atoms. The formed 3D framework structure with void spaces and vacancy sites is occupied by the alkaline ion and zeolitic water.^{23,24} The predicted *Fm-3m* VHCF structure model, in which the O atom replaces the C=N group and the angle of O=V–N is 180°, is optimally selected for powder X-ray diffraction Rietveld refinement for analysis structure parameters of VHCF, and the VHCF lattice parameter is found to be 10.10 Å (see Table S1). The large open framework enables rapid diffusion of a variety of ions. The Fourier transform infrared (FT-IR) and Raman spectrosc-

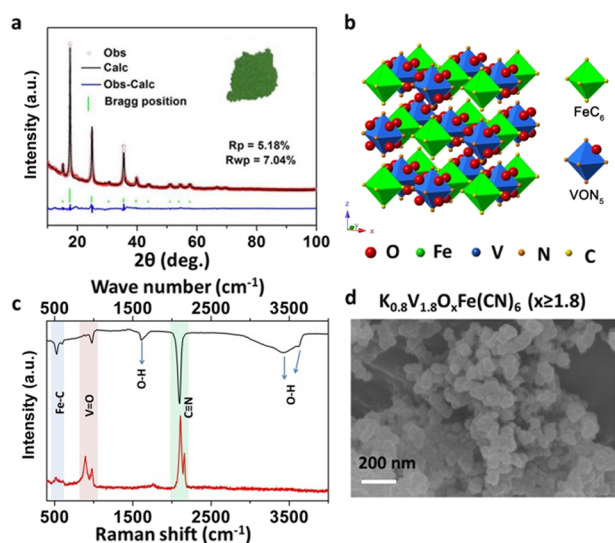


Figure 1. (a) Rietveld refinement of powder X-ray diffraction pattern for VHCF with cubic structure; the inset is a photo of VHCF powder (grass green). (b) Unit cell structure of cubic VHCF with a formula $\text{VOFe}(\text{CN})_6$, which is predicted by ab initio calculations implemented in the CALYPSO code. (c) IR (top) and Raman spectra (bottom) of VHCF powder. (d) SEM image of VHCF powder. Scale bar: 200 nm.

copies of VHCF powder are shown in Figure 1c, which shows three distinctive peaks at 530–600, 900–980, and 2090–2700 cm^{-1} , corresponding to Fe–C stretching,³⁰ V=O,³¹ and C=N stretching, respectively. In addition, the molar ratio of K/V/Fe was determined by inductively coupled plasma optical emission spectroscopy (ICP-OES), indicating that the chemical formula of VHCF was $\text{K}_{0.8}\text{V}_{1.8}\text{O}_x\text{Fe}(\text{CN})_6$ ($x \geq 1.8$). This formula suggests that the mean amount of vacancy, which is formed by the disappearance of $\text{Fe}(\text{CN})_6$ groups, can be occupied by the coordinated zeolite water molecules. As reported in previous work, VHCF could dissolve in $\text{Na}_2\text{SO}_4/3.6 \text{ M H}_2\text{SO}_4$ solution during the electrochemical process. The molar ratio of V/Fe in the electrolyte remained at 3.5 after 250 cycles,²³ illustrating that some V atoms could be easily extracted from VHCF to electrolyte, and those V atoms might not participate in the cubic structural framework. The morphology of VHCF was also characterized by scanning electron microscopy (SEM), showing that the nanoparticle sizes were dispersed from 50 to 150 nm.

3.2. Electrochemical Behaviors of VHCF. The electrochemical behaviors of VHCF in various $\text{Na}^+/\text{HClO}_4$ solutions were investigated. 0.5 M HClO_4 that is much lower than 3.6 M H_2SO_4 solution,^{22,23} together with adding an appropriate amount of polyethylene glycol (PEG),⁷ can ensure VHCF with optimal performances (see Figure 2 and Figures S3–S6). The electrochemical window of the Ti current collector in NaP-4.6 is about 1.9 V (Figure S7). VHCF in the neutral electrolyte decays rapidly during the first 50 cycles, whereas in acid solutions, VHCF exhibits ideal stability performance (Figure S8). So, the existence of H^+ can limit VHCF dissolution, resulting in a H^+ -assisted storage Na^+ -ion reaction. As shown in Figure 2a,b, the reaction with H^+ and Na^+ is complex. There are three sequentially enhanced broad oxidation peaks between 0.4 and 1.45 V and two reduction peaks in the H^+ storage reaction. Two broad oxidation peaks at 1.25 and 1.02 V, together with a weak shoulder peak near 0.70 V, can be seen during the H^+ -assisted Na^+ storage reaction (see Figure 2a).

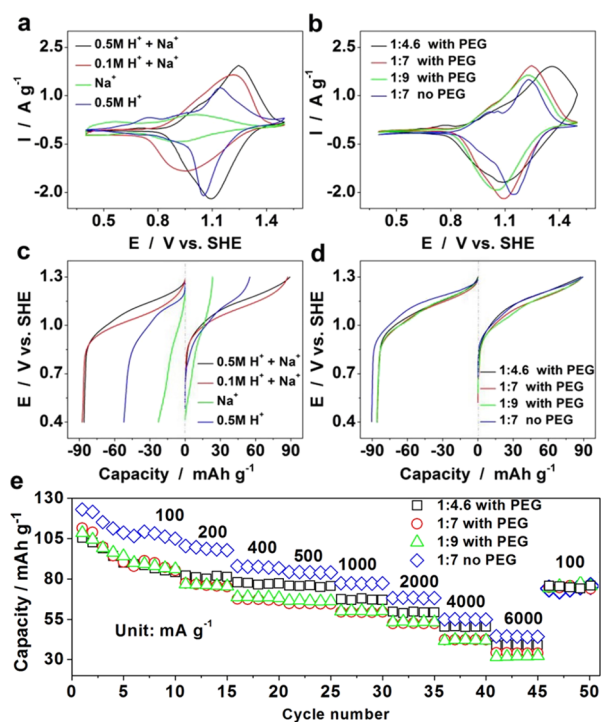


Figure 2. Electrochemical properties of VHCF. (a) Cyclic voltammograms of VHCF in various electrolytes at a scan rate of 2 mV s^{-1} . The black line corresponds to the NaClO_4 electrolyte + 0.5 M HClO_4 . The molar ratio of $[\text{Na}^+]/[\text{H}_2\text{O}]$ is 1:7, and the NaClO_4 electrolyte was prepared by mixing 7 g PEG + 3.96 g NaClO_4 + 6.08 g H_2O . The red line corresponds to the NaClO_4 electrolyte + 0.1 M HClO_4 , and the molar ratio of $[\text{Na}^+]/[\text{H}_2\text{O}]$ is 1:7. The green line corresponds to the NaClO_4 electrolyte. The blue line corresponds to 0.5 M HClO_4 . (b) Cyclic voltammograms of VHCF in Na^+ electrolyte + 0.5 M HClO_4 with various molar ratios of $[\text{Na}^+]/[\text{H}_2\text{O}]$. The scan rate is 2 mV s^{-1} . The black line corresponds to NaP-4.6. The red line corresponds to NaP-7. The green line corresponds to NaP-9. The blue line corresponds to Sat-Na without adding PEG. (c,d) Galvanostatic profiles measured at a current density of 100 mA g^{-1} after 20 cycles of CV at a scan rate of 2 mV s^{-1} for VHCF in various electrolytes corresponding to panels (a) and (b), respectively. (e) Rate capabilities of VHCF operated in NaP-4.6, NaP-7, NaP-9, and Sat-Na; the current densities are 100, 200, 400, 500, 1000, 2000, 4000, and 6000 mA g^{-1} .

These peaks may correspond to Fe(III)/Fe(II) and V(III)/V(IV)/V(V) redox processes, according to the previous result that the valence states of V and Fe ions in the VHCF electrode change by $\text{V}^{3+} \leftrightarrow \text{V}^{4+} \leftrightarrow \text{V}^{5+}$ and $\text{Fe}^{2+} \leftrightarrow \text{Fe}^{3+}$ during the charging/discharging process.^{23,32} In addition, Figure 2c shows that the specific capacity of VHCF in the pure 0.5 M HClO_4 electrolyte is about 52.1 mA h g^{-1} , while in the $\text{NaClO}_4/0.5 \text{ M HClO}_4$ electrolyte (the molar ratio of $[\text{Na}^+]/[\text{H}_2\text{O}]$ is 1:7, named NaP-7), it is 85.6 mA h g^{-1} . That means that only about 33.5 mA h g^{-1} capacity of VHCF is obtained from the Na^+ insertion/extraction reaction in the NaP-7 electrolyte. This indicates that VHCF has higher storage ability with H^+ than with Na^+ and about 60.9% capacity is harvested from H^+ storage. More importantly, the synergistic action of H^+ and Na^+ can strongly inhibit the dissolution process of VHCF (see Figure S8). Moreover, the specific capacity of VHCF in the $\text{Na}^+/0.5 \text{ M HClO}_4$ electrolyte is nearly not affected by the molar ratio of $[\text{Na}^+]/[\text{H}_2\text{O}]$ when adding a certain amount of PEG in the electrolyte despite the polarization of VHCF in

NaP-4.6 being the largest among all the experimented electrolytes (see Figure 2b,d). However, the VHCF electrode in the saturated NaClO₄ electrolyte ([Na⁺]/[H₂O] = 1:7) without PEG exhibits the highest capacity (90.4 mA h g⁻¹) at 100 mA g⁻¹, which may be induced by the high conductivity of the Sat-Na electrolyte. From Figure 2b, we find that the overpotential increases slightly after adding PEG in electrolytes with a [Na⁺]/[H₂O] molar ratio of 1:7 (also see Figure S9a). This can be ascribed to the reduced Na⁺-ion concentration and PEG–Na⁺ coordination after adding PEG, both of which lead to a lower ion conduction in the bulk electrolyte with PEG (see Figure S9b) and thus to a higher overpotential. In Figure 2b, we also find that the overpotential of the VHCF electrode in the PEG-containing electrolyte has a downward trend with increasing molar ratio of [H₂O]/[Na⁺] from 4.6 to 9 (also see Figure S9a). As seen from Figure S9b, the NaClO₄ electrolyte with PEG of low water content exhibits relatively low ion conductivity, although it has a higher Na⁺ concentration and thus has a higher overpotential. Since Na⁺ ions can coordinate with PEG, more Na⁺ ions coordinate with PEG as the molar ratio of [H₂O]/[Na⁺] decreases, which leads to the overall reduced conductivity.

Interestingly, the VHCF electrode in NaP-4.6 exhibits the best rate capability retentions despite NaP-4.6 being the lowest conductivity when the electrolyte contains PEG, as indicated in Figure 2e. Although the capacity performance of the VHCF electrode in Sat-Na is the best, due to the high conductivity of the Sat-Na electrolyte, the capacity retentions of the VHCF electrode in SaP-4.6 are 79.2 and 46.0% at 1000 and 6000 mA g⁻¹, respectively, which are higher than the corresponding values in Sat-Na (73.3 and 41.9% at the same current densities, respectively). It is obvious that the introduced PEG is beneficial to the high-rate and long-term capability of the VHCF electrode when the molar ratio of [H₂O]/[Na⁺] reaches about 4.6 (also see Figure 3). This is because the donor with a lone pair of oxygen atoms in PEG can form Na⁺ coordination to increase the solubility of metal salts,³³ and this Na⁺–PEG coordination can be formed when the solution has a low water component,^{34,35} but a higher water component ([H₂O]/[Na⁺] = 7, 9) results in a weakened Na⁺–PEG coordination caused by H₂O competition. Moreover, according to the galvanostatic profiles of the VHCF electrode in Figure 3, about 93.1% of the initial discharge capacity can be obtained after 1000 cycles at a current density of 1000 mA g⁻¹ in NaP-4.6, which is 13.1% higher than that in Sat-Na (about 80.2% discharge capacity retention). In NaP-7, the capacity retention is about 90.6%, indicating that the lower water content and PEG addition can improve the stability of the VHCF electrode. Thus, it is clear that the formed Na⁺-coordinated PEG can adsorb on the surface of the VHCF electrode, which can not only provide a Na⁺ transport channel between the solid electrode and liquid electrolyte but also prohibit the direct contact of the liquid electrolyte with the solid electrode. The latter might stabilize the solid VHCF electrode. The galvanostatic charge/discharge of the VHCF/NaP-4.6/WO₃ battery operated ranges from 0.1 to 1.0 V at a current density of 800 mA g⁻¹ (see Figure 3d), and the working voltage of the battery was found to be 0.62 V. The WO₃ anode that has a capacity of about 95 mA h g⁻¹ at a current density of 100 mA g⁻¹ in the NaP-4.6 electrolyte is where the intercalation and electrochromic reactions of Na⁺ and H⁺ occur (see Figures S10–S12) as the VHCF cathode releases and stores H⁺ and Na⁺ during the charging/

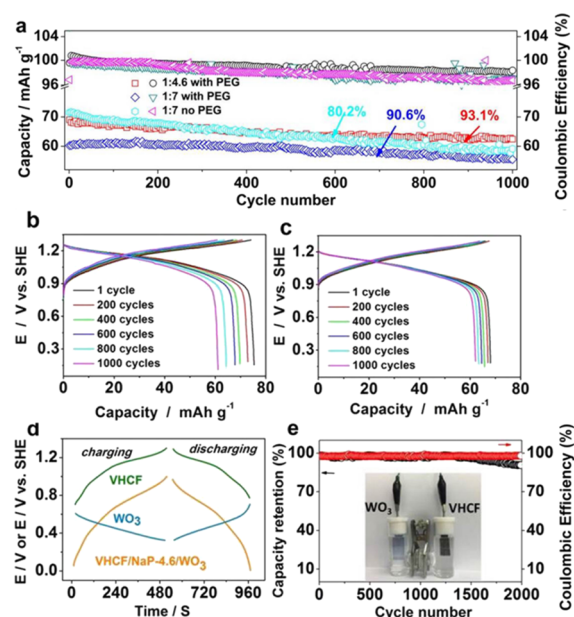


Figure 3. Stability performances of VHCF electrodes in various electrolytes at a current density of 1000 mA g⁻¹. (a) VHCF operated in NaP-4.6, NaP-7, and Sat-Na in a three-electrode cell. (b) Galvanostatic profiles of VHCF in a three-electrode cell operated in Sat-Na; the molar ratio of [Na⁺]/[H₂O] is 1:7. (c) Galvanostatic profiles of VHCF in a three-electrode cell operated in NaP-4.6, which is nearly saturated NaClO₄ + 0.5 M HClO₄. (d) Galvanostatic profiles of VHCF/NaP-4.6/WO₃ battery along with the voltage profiles of their individual anode and cathode electrodes vs SHE at a current density of 1000 mA g⁻¹. (e) Stability performance of VHCF/NaP-4.6/WO₃ battery at a current density of 1000 mA g⁻¹; the inset is a photo of the battery in an H-type cell. The charging and discharging process is shown in Video S1.

discharging process. According to the previous works,^{23,32,36} in the VHCF cathode electrode, V(III) + H₂O → [V(IV)O]²⁺ + 2H⁺ + e⁻, Fe(II) → Fe(III) + e⁻, and [V(IV)O₂H]⁺ → [V(V)O₂]⁺ + e⁻ + H⁺ reactions occur; the reactions that occurred in the WO₃ anode include W(VI) + xH⁺ + xe⁻ → H_xWO₃ and W(VI) + xNa⁺ + xe⁻ → Na_xWO₃. The stability of VHCF during cycling at a current density of 1000 mA g⁻¹ is shown in Figure 3e, and about 90.3% of the initial discharge capacity was obtained after 2000 cycles, which is the second highest on record among the RAIBs based on Na⁺ shuttles with ideal energy density (17 Wh kg⁻¹) (see Table S2). The side reaction of water electrolysis was limited at such high current density; this is propitious to increase the coulombic efficiency, which decreased from 98.9 to 97.8% during the cycling process. Furthermore, the interfacial chemistry was also investigated by the solid-state NMR technology as discussed in the following section.

3.3. Interphase of VHCF Electrodes. The ¹H and ²³Na NMR spectra of VHCF samples both with washing and without washing by ethanol were obtained in NaP-4.6 solution as shown in Figure 4. The ¹H NMR signals of VHCF in Na acid solution show resonances that can be assigned to PEG (3.5 ppm). Two sharp ²³Na signals at -19.5 and -20.7 ppm observed in NMR spectra of VHCF samples correspond to the central transition of ²³Na in NaClO₄ crystals,³⁷ while a relatively broad ²³Na signal at -10.8 ppm is obviously different from both the lattice Na⁺ (-42.2 ppm, see below) of VHCF and Na⁺ of NaClO₄ and can be assigned to the PEG–Na⁺

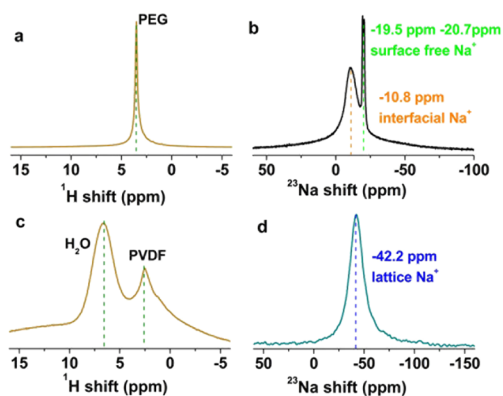


Figure 4. ^1H and ^{23}Na solid-state NMR spectra at 14 KHz of individual VHCfs, obtained after 20 cyclic voltammetry cycles at a scan rate of 2 mV s^{-1} in NaP-4.6. (a,c) ^1H ssNMR spectra of VHCF electrode. (b,d) ^{23}Na ssNMR spectra of VHCF electrode. (a,b) The VHCF sample was obtained without ethanol washing. (c,d) The VHCF sample was obtained by fully washing with ethanol several times.

complex deposited on the surface of the VHCF electrode. The appearance of complex PEG– Na^+ on the surface of the VHCF electrode not only provides a passageway for Na^+ ions entering the VHCF electrode from the electrolyte but also can effectively prevent VHCF from contacting water in the electrolyte and thus limit the solubility of VHCF.

3.4. Intercalation Reaction of VHCF Electrode. The mechanisms of the Na^+ reaction was further investigated by solid-state NMR and kinetic analysis (see Figure 5b–d). The ex situ XRD patterns (Ti (101) peak as the internal standard) were also detected to get the structure characteristics of VHCF during the galvanostatic process. As shown in Figure 5a and Figure S10, the VHCF electrode can maintain its initial cubic structure during charge/discharge, indicating that the crystal structure of VHCF does not change during the extraction and embedding processes. However, during the charging process, the XRD peaks of (200) and (220) as well as (422) shift to low angles from oxidation States a to c and then slightly shift toward the high angle from oxidation State c to State d. Reverse variations occur during the discharging process (see Figure 5c and Figures S13–S14, Table S3). The above result illustrates that, during the charging process, the lattice first expands and then contracts slightly. The lattice expansions and contractions along the three directions are small, for example, about 0.8% from States a to c and 0.1% from States c to d, which are close to zero strain. We tentatively interpret above lattice expansion or contraction as follows. During the charging process, the energy of the Fe(II)/Fe(III) couple is controlled by the π -bonding Fe–C interaction, and the V(III)/V(IV) or V(IV)/V(V) couple is controlled by the O=V–N interaction. The Fe...V distance is affected by the cooperative rotation from the linear Fe–C \equiv N–V=O axis. From States a to c, the rotation of the linear (–C \equiv N–) leads to the slight elongations in both Fe–C and V–N bonds,³⁸ giving rise to the lattice expansion. This may be caused by the oxidation of Fe(II) to Fe(III) and V(III) to V(IV). However, the slight lattice contraction from States c to d may be due to the reaction of V(IV)/V(V) couples accompanied by the H^+ storage reaction.

The ex situ ^{23}Na solid NMR spectra at different oxidation states of VHCF upon the galvanostatic process (States a to g)

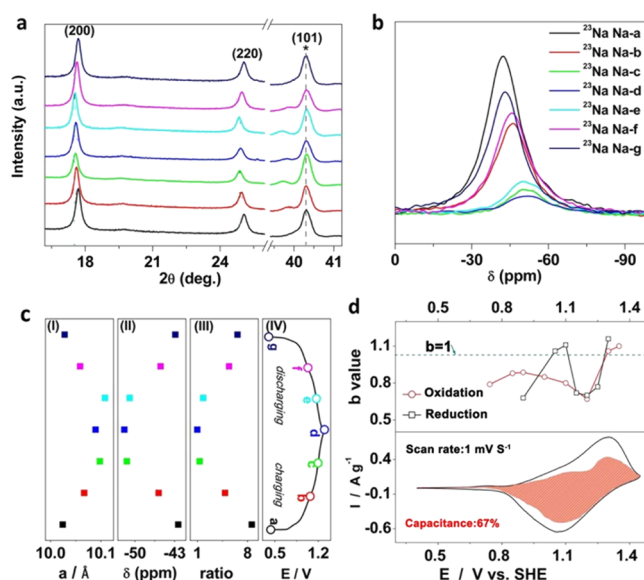


Figure 5. (a) Ex situ XRD patterns of VHCF electrode at different charging/discharging states in which the Ti (101) peak is used as the internal standard for XRD patterns. (b) Ex situ ^{23}Na solid-state NMR spectra of Na-ion content in VHCF with cycling obtained by quantitative analysis of ^{23}Na NMR. (c) Changes of lattice parameter (I), chemical shift ^{23}Na solid-state NMR (II), area of ^{23}Na NMR quantitative analysis spectra ratio (area of Na-a-g/area of Na-d) (III), and VHCF electrochemical cycling (IV). Seven states, namely, a (0.433 V), b (1.070 V), c (1.197 V), d (1.300 V), e (1.169 V), f (1.033 V), and g (0.399 V), are selected for comparison. (d) b values at different oxidation/reduction states (top) and cyclic voltammogram with the capacitive contribution (the red region) to the total current for VHCF (bottom).

were further used to monitor the extraction/embedding of Na^+ ions during the charging/discharging processes. Figure 5b shows the quantitative ^{23}Na ssNMR spectra of different VHCfs at various cutoff voltages (the spectra of different VHCfs were divided by their own weights). The mathematical areas of ex situ ^{23}Na NMR spectra are related to the content changes of Na^+ in VHCF during charging/discharging processes, which can be used to approximately characterize the quantitative variation of Na^+ content during the charging and discharging. As revealed in Figure 5b, the ^{23}Na signal of VHCF is upfield shifted about 10.51 ppm (from -42.35 to -52.86 ppm) in the charging process (States a to d), but only a shift of 0.46 ppm occurs from States c to d. During the discharging process (States d–g), the ^{23}Na chemical shift moves back to the initial State a, suggesting that the reversible redox reactions occur during charge and discharge processes with H^+ and Na^+ storage reactions. The area ratio of Na-n/Na-d ($n = \text{a–g}$) has the same trend with the ^{23}Na chemical shift. The Na^+ content drops dramatically from State a to State c during charging, which is characterized by area ratio variation of Na-n/Na-d from 8.6 to 1.3. During the subsequent charging process from States c to d, however, the Na content decreases little (the area ratio changes from 1.3 to 1). That is to say, about 96% of Na^+ ions are extracted from VHCF during the charging process from State a to State c, and only 4% of Na^+ ions are extracted during the subsequent charge process from State c to State d. Reverse variations of Na^+ content are observed during the discharging process. The above results imply that the Na^+ storage reaction mainly occurs during the State a to c (or State e to g) process while the H^+ storage

reaction mainly occurs during States c to d and d to e processes (see Figure 5c). From Figure 2, it is calculated that only about 39.1% capacity was from the Na⁺ storage reaction, indicating that, during the States a to c charge processes, about 2/3 capacity storage in VHCF was accompanied by Na⁺ and H⁺ reactions, and the 1/3 capacity storage during States c to d was mainly from the H⁺ reaction that is supposed to be accompanied by the oxidation of V(IV)/V(V) couples.

Kinetic analysis of VHCF for the H⁺ and Na⁺ storage reactions is shown in Figure 5d, indicating that about 67% capacitive current contributes to the total current of VHCF at 1 mV s⁻¹. A high capacitive percentage is generally contributed by the fast diffusion rates and short diffusion distances,³⁹ resulting from the low reaction activation energy. The *b* values are the slopes of log(peak current) versus log(sweep rate) as shown in Figure S15 and Table S4. When *b* = 1.0, the current belongs to capacitive behavior that is not diffusion-limited, and when *b* = 0.5, the current is limited by the semi-infinite linear diffusion.^{40,41} However, the average *b* value during the charging process is observed to be about 0.85 between 0.65 and 1.10 V (vs SHE) and drops to 0.67 at 1.2 V (State c, *V* = 1.197 V) and then increases to 1.0 when the voltage is higher than 1.3 V. In addition, the average *b* value is about 0.7 between 1.15 and 1.25 V (State e, *V* = 1.169 V) during the reduction process, which is lower than those at other voltages. These observations indicate that the H⁺ storage reaction accompanied by the reaction of V(IV)/V(V) couples near States c and e may be a two-step reaction. The first step may be the adsorption of the zeolite water,³² which has a slightly higher activation energy than the second reaction.

Overall, the results discussed above suggest that the H⁺ storage reaction should be accounted for the redox of V(III)/V(IV) and V(IV)/V(V) couples and Na⁺ intercalation should be accounted for the redox of the Fe(II)/Fe(III) couple.

4. CONCLUSIONS

In summary, the VHCF/WO₃ aqueous sodium battery exhibits an ultrahigh stability at a high current density of 1000 mA g⁻¹ and about 90.1% capacity retention after 2000 cycles in NaP-4.6 electrolyte. The slight structural deformations induced by the cation intercalation and PEG–Na⁺ interphase are the main contributors to both the excellent electrochemical stability and the improved capacity capability. The Na⁺-intercalation chemistry in the VHCF electrode is revealed by ²³Na ssNMR spectra and XRD. Our ssNMR result reveals that most Na⁺ ions (~96%) are extracted from VHCF during the first 2/3 charging process and only a very small amount of Na⁺ ions is extracted during the subsequent 1/3 charging process. It is suggested that both iron and vanadium atoms in VHCF are the centers involved in the redox reaction accompanying the reversible storage reactions of Na⁺ and H⁺. The H⁺ storage reaction is likely accompanied by the redox of vanadium atoms, and Na⁺ intercalation is accompanied by the redox of iron atoms. The results of the ssNMR study offer new insights into the intercalation chemistry of Prussian blue analogues (PBAs) with open-framework-structured compounds, which can greatly broaden our horizons for battery research.

■ ASSOCIATED CONTENT

Supporting Information

The Supporting Information is available free of charge on the ACS Publications website at DOI: 10.1021/acsami.9b04849.

Experimental section and other characterizations and electrochemical performances (PDF)

Charging/discharging of the battery (AVI)

■ AUTHOR INFORMATION

Corresponding Authors

*E-mail: jiujun@shaw.ca (J.Z.).

*E-mail: liuzp@nimte.ac.cn (Z.L.).

*E-mail: jwfeng@wipm.ac.cn (J.F.).

ORCID

Yanchao Wang: 0000-0003-4518-925X

Jiujun Zhang: 0000-0002-6858-4060

Zhaoping Liu: 0000-0002-3943-8953

Jiwen Feng: 0000-0002-9691-8574

Author Contributions

#P.J. and Z.L. contributed equally to this work. Z.L. performed ssNMR experiments. X.S. and Y.W. performed ab initio structure predictions.

Funding

National Natural Science Foundation of China and Youth Innovation Promotion Association CAS.

Notes

The authors declare no competing financial interest.

■ ACKNOWLEDGMENTS

The authors thank the kind supply of ab initio calculations from Yanming Ma's Group (Jilin University). This work was supported by the National Natural Science Foundation of China (Grant Nos. 11474314, 21603267, 51872305) and Youth Innovation Promotion Association CAS (Grant No. 2017341).

■ REFERENCES

- (1) Kameda, Y.; Saito, S.; Umabayashi, Y.; Fujii, K.; Amo, Y.; Usuki, T. Local structure of Li⁺ in concentrated LiPF₆-dimethyl carbonate solutions. *J. Mol. Liq.* **2016**, *217*, 17–22.
- (2) Goodenough, J. B.; Kim, Y. Challenges for Rechargeable Li Batteries. *Chem. Mater.* **2010**, *22*, 587–603.
- (3) Soloveichik, G. L. Battery Technologies for Large-Scale Stationary Energy Storage. In *Annual Review of Chemical and Biomolecular Engineering, Vol 2*, Prausnitz, J. M., Ed.; 2011, Vol. 2, pp 503–527.
- (4) Dunn, B.; Kamath, H.; Tarascon, J.-M. Electrical Energy Storage for the Grid: A Battery of Choices. *Science* **2011**, *334*, 928–935.
- (5) Alias, N.; Mohamad, A. A. Advances of aqueous rechargeable lithium-ion battery: A review. *J. Power Sources* **2015**, *274*, 237–251.
- (6) Bin, D.; Wang, F.; Tamirat, A. G.; Suo, L.; Wang, Y.; Wang, C.; Xia, Y. Progress in Aqueous Rechargeable Sodium-Ion Batteries. *Adv. Energy Mater.* **2018**, *8*, 1703008.
- (7) Niu, L.; Chen, L.; Zhang, J.; Jiang, P.; Liu, Z. Revisiting the open-framework zinc hexacyanoferrate: The role of ternary electrolyte and sodium-ion intercalation mechanism. *J. Power Sources* **2018**, *380*, 135–141.
- (8) Paulitsch, B.; Yun, J.; Bandarenka, A. S. Electrodeposited Na₂VO_x[Fe(CN)₆] films As a Cathode Material for Aqueous Na-Ion Batteries. *ACS Appl. Mater. Interfaces* **2017**, *9*, 8107–8112.
- (9) Pasta, M.; Wang, R. Y.; Ruffo, R.; Qiao, R.; Lee, H.-W.; Shyam, B.; Guo, M.; Wang, Y.; Wray, L. A.; Yang, W.; Toney, M. F.; Cui, Y. Manganese-cobalt hexacyanoferrate cathodes for sodium-ion batteries. *J. Mater. Chem. A* **2016**, *4*, 4211–4223.
- (10) Chen, L.; Shao, H.; Zhou, X.; Liu, G.; Jiang, J.; Liu, Z. Water-mediated cation intercalation of open-framework indium hexacyanoferrate with high voltage and fast kinetics. *Nat. Commun.* **2016**, *7*, 11982.

- (11) Zhang, L.; Chen, L.; Zhou, X.; Liu, Z. Towards High-Voltage Aqueous Metal-Ion Batteries Beyond 1.5 V: The Zinc/Zinc Hexacyanoferrate System. *Adv. Energy Mater.* **2015**, *5*, 1400930.
- (12) Wu, X.; Sun, M.; Guo, S.; Qian, J.; Liu, Y.; Cao, Y.; Ai, X.; Yang, H. Vacancy-Free Prussian Blue Nanocrystals with High Capacity and Superior Cyclability for Aqueous Sodium-Ion Batteries. *ChemNanoMat* **2015**, *1*, 188–193.
- (13) Pasta, M.; Wessells, C. D.; Liu, N.; Nelson, J.; McDowell, M. T.; Huggins, R. A.; Toney, M. F.; Cui, Y. Full open-framework batteries for stationary energy storage. *Nat. Commun.* **2014**, *5*, 3007.
- (14) Lee, H.-W.; Wang, R. Y.; Pasta, M.; Lee, S. W.; Liu, N.; Cui, Y. Manganese hexacyanomanganate open framework as a high-capacity positive electrode material for sodium-ion batteries. *Nat. Commun.* **2014**, *5*, 5280.
- (15) Takachi, M.; Matsuda, T.; Moritomo, Y. Cobalt Hexacyanoferrate as Cathode Material for Na + Secondary Battery. *Appl. Phys. Express* **2013**, *6*, No. 025802.
- (16) Pasta, M.; Wessells, C. D.; Huggins, R. A.; Cui, Y. A high-rate and long cycle life aqueous electrolyte battery for grid-scale energy storage. *Nat. Commun.* **2012**, *3*, 1149.
- (17) Wessells, C. D.; Peddada, S. V.; Huggins, R. A.; Cui, Y. Nickel hexacyanoferrate nanoparticle electrodes for aqueous sodium and potassium ion batteries. *Nano Lett.* **2011**, *11*, 5421–5425.
- (18) Wessells, C. D.; Huggins, R. A.; Cui, Y. Copper hexacyanoferrate battery electrodes with long cycle life and high power. *Nat. Commun.* **2011**, *2*, 550.
- (19) Yan, P.; Zheng, J.; Liu, J.; Wang, B.; Cheng, X.; Zhang, Y.; Sun, X.; Wang, C.; Zhang, J.-G. Tailoring grain boundary structures and chemistry of Ni-rich layered cathodes for enhanced cycle stability of lithium-ion batteries. *Nat. Energy* **2018**, *3*, 600–605.
- (20) Mohamed, A. I.; Sansone, N. J.; Kuei, B.; Washburn, N. R.; Whitacre, J. F. Using Polypyrrole Coating to Improve Cycling Stability of $\text{NaTi}_2(\text{PO}_4)_3$ as an Aqueous Na-Ion Anode. *J. Electrochem. Soc.* **2015**, *162*, A2201–A2207.
- (21) Yamada, Y.; Furukawa, K.; Sodeyama, K.; Kikuchi, K.; Yaegashi, M.; Tateyama, Y.; Yamada, A. Unusual Stability of Acetonitrile-Based Superconcentrated Electrolytes for Fast-Charging Lithium-Ion Batteries. *J. Am. Chem. Soc.* **2014**, *136*, 5039–5046.
- (22) Chen, X.; Cao, B.; Liu, H.; Xu, B.; Lei, Y.; Song, H. Mesoporous soft carbon as an anode material for sodium ion batteries with superior rate and cycling performance. *J. Mater. Chem. A* **2016**, *4*, 6472–6478.
- (23) Lee, J.-H.; Ali, G.; Kim, D. H.; Chung, K. Y. Metal-Organic Framework Cathodes Based on a Vanadium Hexacyanoferrate Prussian Blue Analogue for High-Performance Aqueous Rechargeable Batteries. *Adv. Energy Mater.* **2017**, *7*, 1601491.
- (24) Wardecki, D.; Ojwang, D. O.; Grins, J.; Svensson, G. Neutron Diffraction and EXAFS Studies of $\text{K}_{2x/3}\text{Cu}[\text{Fe}(\text{CN})_6]_2 \cdot n\text{H}_2\text{O}$. *Cryst. Growth Des.* **2017**, *17*, 1285–1292.
- (25) Wu, X.-y.; Sun, M.-y.; Shen, Y.-f.; Qian, J.-f.; Cao, Y.-l.; Ai, X.-p.; Yang, H.-x. Energetic Aqueous Rechargeable Sodium-Ion Battery Based on $\text{Na}_2\text{CuFe}(\text{CN})_6\text{-NaTi}_2(\text{PO}_4)_3$ Intercalation Chemistry. *ChemSusChem* **2014**, *7*, 407–411.
- (26) Ma, Y.; Eremets, M.; Oganov, A. R.; Xie, Y.; Trojan, I.; Medvedev, S.; Lyakhov, A. O.; Valle, M.; Prakapenka, V. Transparent dense sodium. *Nature* **2009**, *458*, 182–185.
- (27) Li, Y.; Feng, X.; Liu, H.; Hao, J.; Redfern, S. A. T.; Lei, W.; Liu, D.; Ma, Y. Route to high-energy density polymeric nitrogen t-N via He-N compounds. *Nat. Commun.* **2018**, *9*, 722.
- (28) Wang, Y.; Lv, J.; Zhu, L.; Ma, Y. Crystal structure prediction via particle-swarm optimization. *Phys. Rev. B* **2010**, *82*, No. 094116.
- (29) Wang, Y.; Lv, J.; Zhu, L.; Ma, Y. CALYPSO: A method for crystal structure prediction. *Comput. Phys. Commun.* **2012**, *183*, 2063–2070.
- (30) Barsan, M. M.; Butler, I. S.; Fitzpatrick, J.; Gilson, D. F. R. High-pressure studies of the micro-Raman spectra of iron cyanide complexes: Prussian blue ($\text{Fe}_4[\text{Fe}(\text{CN})_6]_3$), potassium ferricyanide ($\text{K}_3[\text{Fe}(\text{CN})_6]$), and sodium nitroprusside ($\text{Na}_2[\text{Fe}(\text{CN})_5(\text{NO}) \cdot 2\text{H}_2\text{O}]$). *J. Raman Spectrosc.* **2011**, *42*, 1820–1824.
- (31) Tsiafoulis, C. G.; Trikalitis, P. N.; Prodromidis, M. I. Synthesis, characterization and performance of vanadium hexacyanoferrate as electrocatalyst of H_2O_2 . *Electrochem. Commun.* **2005**, *7*, 1398–1404.
- (32) Shaojun, D.; Fengbin, L. Researches on chemically modified electrodes: Part XV. Preparation and electrochromism of the vanadium hexacyanoferrate film modified electrode. *J. Electroanal. Chem. Interfacial Electrochem.* **1986**, *210*, 31–44.
- (33) Henderson, W. A.; McKenna, F.; Khan, M. A.; Brooks, N. R.; Young, V. G., Jr.; Frech, R. Glyme-lithium bis-(trifluoromethanesulfonyl)imide and glyme-lithium bis-(perfluoroethanesulfonyl)imide phase behavior and solvate structures. *Chem. Mater.* **2005**, *17*, 2284–2289.
- (34) Li, Y.; Liang, Y.; Hernandez, F. C. R.; Yoo, H. D.; An, Q.; Yao, Y. Enhancing sodium-ion battery performance with interlayer-expanded MoS_2 -PEO nanocomposites. *Nano Energy* **2015**, *15*, 453–461.
- (35) Luo, H.; Liang, X.; Feng, J.; Wang, L. Segmental Motion of PEO₈:NaPF₆ Crystalline Polymer Electrolyte. *Chin. J. Magn. Reson.* **2015**, *32*, 12–22.
- (36) Cai, G.; Cui, M.; Kumar, V.; Darmawan, P.; Wang, J.; Wang, X.; Lee-Sie Eh, A.; Qian, K.; Lee, P. S. Ultra-large optical modulation of electrochromic porous WO_3 film and the local monitoring of redox activity. *Chem. Sci.* **2016**, *7*, 1373–1382.
- (37) Sawers, L. J. M.; Tunstall, D. P.; Bruce, P. G. An NMR investigation of the formation of the crystalline complex $(\text{PEO})_3\text{NaClO}_4$. *Solid State Ionics* **1998**, *107*, 13–23.
- (38) You, Y.; Wu, X.-L.; Yin, Y.-X.; Guo, Y.-G. High-quality Prussian blue crystals as superior cathode materials for room-temperature sodium-ion batteries. *Energy Environ. Sci.* **2014**, *7*, 1643–1647.
- (39) Lesel, B. K.; Ko, J. S.; Dunn, B.; Tolbert, S. H. Mesoporous $\text{Li}_x\text{Mn}_2\text{O}_4$ Thin Film Cathodes for Lithium-Ion Pseudocapacitors. *ACS Nano* **2016**, *10*, 7572–7581.
- (40) Augustyn, V.; Come, J.; Lowe, M. A.; Kim, J. W.; Taberna, P.-L.; Tolbert, S. H.; Abruña, H. D.; Simon, P.; Dunn, B. High-rate electrochemical energy storage through Li^+ intercalation pseudocapacitance. *Nat. Mater.* **2013**, *12*, 518–522.
- (41) Brezesinski, T.; Wang, J.; Tolbert, S. H.; Dunn, B. Ordered mesoporous $\alpha\text{-MoO}_3$ with iso-oriented nanocrystalline walls for thin-film pseudocapacitors. *Nat. Mater.* **2010**, *9*, 146–151.